



Accurate and Efficient Photoeccentric Transit Modeling

Mason G. MacDougall¹, Gregory J. Gilbert¹, and Erik A. Petigura¹Department of Physics & Astronomy, University of California Los Angeles, Los Angeles, CA 90095, USA; macdougall@astro.ucla.edu

Received 2023 April 21; revised 2023 June 15; accepted 2023 June 23; published 2023 July 14

Abstract

A planet’s orbital eccentricity is fundamental to understanding the present dynamical state of a system and is a relic of its formation history. There is high scientific value in measuring the eccentricities of Kepler and Transiting Exoplanet Survey Satellite (TESS) planets given the sheer size of these samples and the diversity of their planetary systems. However, Kepler and TESS light curves typically only permit robust determinations of the planet-to-star radius ratio r , orbital period P , and transit midpoint t_0 . Three other orbital properties, including the impact parameter b , eccentricity e , and argument of periastron ω , are more challenging to measure because they are all encoded in the light curve through subtle effects on a single observable—the transit duration T_{14} . In Gilbert et al., we showed that a five-parameter transit description $\{P, t_0, r, b, T_{14}\}$ naturally yields unbiased measurements of r and b . Here, we build upon our previous work and introduce an accurate and efficient prescription to measure e and ω . We validate this approach through a suite of injection-and-recovery experiments. Our method agrees with previous approaches that use a seven-parameter transit description $\{P, t_0, r, b, \rho_*, e, \omega\}$, which explicitly fits the eccentricity vector and mean stellar density. The five-parameter method is simpler than the seven-parameter method and is “future-proof” in that posterior samples can be quickly reweighted (via importance sampling) to accommodate updated priors and updated stellar properties. This method thus circumvents the need for an expensive reanalysis of the raw photometry, offering a streamlined path toward large-scale population analyses of the eccentricity from transit surveys.

Unified Astronomy Thesaurus concepts: [Exoplanets \(498\)](#); [Transit photometry \(1709\)](#); [Bayesian statistics \(1900\)](#); [Eccentricity \(441\)](#); [Light curves \(918\)](#); [Astronomy data modeling \(1859\)](#)


1. Introduction

Out of more than 5300 confirmed planets to date, $\sim 75\%$ were discovered via the transit method. These discoveries have paved the way for keystone scientific advancements in our understanding of planet formation, evolution, and demographics. To ensure the reliability of inferences based on the transiting planet population, we must also ensure that characterizations of individual transiting planets are consistently and accurately derived. Previously, uncertainties on stellar parameters significantly limited the achievable precision of planet properties (e.g., $\sigma(R_*) \sim 27\%$ and $\sigma(\rho_*) \sim 51\%$; Thompson et al. 2018). Now, in the era of Gaia (Collaboration et al. 2018) and high-precision stellar characterizations (e.g., $\sigma(R_*) \lesssim 2\%$ and $\sigma(\rho_*) \lesssim 10\%$), the determination of key planet properties is limited by light-curve modeling (see, e.g., Petigura 2020).

A variety of methods exist for modeling transit signals, including various parameterizations (e.g., Seager & Mallén-Ornelas 2003; Carter et al. 2008; Dawson & Johnson 2012; Eastman et al. 2013; Thompson et al. 2018; Gilbert et al. 2022) and sampling techniques (e.g., Feroz & Hobson 2008; Foreman-Mackey et al. 2013; Foreman-Mackey et al. 2021; Speagle 2020; Gilbert 2022). Differences in posterior inference, which arise from adopting a particular model parameterization and sampling method, are often assumed to be insignificant relative to other sources of uncertainty. However, if one wishes to achieve percent-level precision on all quantities, one must also carefully consider the strengths and weaknesses of competing model/sampler implementations (see, e.g., Gilbert

et al. 2022; Gilbert 2022). Although substantial effort has been put into vetting methods for transit signal detection (see, e.g., Christiansen et al. 2015), far less effort has been devoted to validating subsequent methods for transit signal modeling. A key aim of this work—which builds directly upon our previous work in Gilbert et al. 2022, hereafter **G22**—is to place the transit modeling problem on the same secure foundation as the transit detection problem. Our primary focus here is on the effects of model parameterization, with a secondary focus on the role of the sampler.

A popular and straightforward method for transit model parameterization is to use a seven-parameter basis that includes the orbital period P , transit epoch t_0 , planet-to-star radius ratio r , impact parameter b , eccentricity e , argument of periastron ω , and either the stellar density ρ_* or scaled orbital separation a/R_* , with these latter two parameters being related via Kepler’s third law¹ (see, e.g., Eastman et al. 2013). This eccentricity-explicit basis $\{P, t_0, r, b, e, \omega, \rho_*\}$, $e-\omega-\rho$ hereafter, benefits from being fully characterized by properties of the star, planet, and planetary orbit. However, real-world photometric transit light curves typically only include enough information to constrain four or five out of the seven parameters. More precisely, in most real-world cases the signal-to-noise ratio (S/N) of observations is low enough that one cannot precisely measure the duration and curvature of ingress/egress nor can one detect any transit asymmetry (see Barnes 2007). Without resolved ingress/egress or transit asymmetry, the problem remains unconstrained, with b, e, ω ,

 Original content from this work may be used under the terms of the [Creative Commons Attribution 4.0 licence](https://creativecommons.org/licenses/by/4.0/). Any further distribution of this work must maintain attribution to the author(s) and the title of the work, journal citation and DOI.

¹ In practice, other parameters related to the stellar limb darkening (i.e., quadratic limb darkening coefficients u_1, u_2) and to the properties of the photometry (i.e., flux zero-point F_0 and photometric noise σ_F) are usually also needed, but these complicating details are not the focus of this paper.

and ρ_* each imprinting themselves on the light curve indirectly via the transit duration T_{14} (r imprints itself via the transit depth; P and t_0 via the ephemeris). More explicitly, for a given ρ_* , b influences the transit chord length, e and ω influence the speed of the planet during transit, and the ratio of transit chord length to orbital speed produces T_{14} .

An alternative approach that improves upon these limitations of the seven-parameter method is to model the light curve assuming a circular orbit, $e = 0$, regardless of what the true underlying eccentricity might be (see, e.g., Seager & Mallén-Ornelas 2003; Dawson & Johnson 2012). This shortcut reduces the total number of model parameters by two with a trade-off that the transit is now explicitly assumed to be symmetric. Fortunately, for virtually all Kepler and Transiting Exoplanet Survey Satellite class photometry, this assumption does not introduce measurable biases into the analysis. In G22, we explored the effectiveness of two different five-parameter bases: $\{P, t_0, r, b, T_{14}\}$ versus $\{P, t_0, r, b, \tilde{\rho}\}$, where $\tilde{\rho}$ is the stellar pseudo-density, i.e., the stellar density inferred from the transit photometry under the (probably false) assumption of a circular orbit. We found that the two bases are equivalent when an appropriate Jacobian transformation is properly applied, but that the latter basis introduces complex, nonintuitive covariances between b and $\tilde{\rho}$. These covariances artificially disfavor $b \gtrsim 0.7$, which propagates through to other parameters, shifting e toward higher values and r toward lower ones. Historically, the use of parameter bases, which include $\tilde{\rho}$ has resulted in biased inference, and we consequently recommend avoiding the use of $\tilde{\rho}$ altogether. For the remainder of this work, we therefore do not consider any parameterizations which include $\tilde{\rho}$.

Our preferred model parameterization $\{P, t_0, r, b, T_{14}\}$, hereafter the T_{14} basis, benefits from being intuitive and close to quantities that can be directly measured from the transit photometry, which minimizes the risk of introducing unintended bias. In G22, we demonstrated that this parameterization yields unbiased posteriors on both b and T_{14} . In this work, we build on G22 to develop a post-hoc importance sampling routine that enables indirect recovery of e and ω from direct measurements of T_{14} and an independent external constraint on ρ_* (e.g., from asteroseismology or spectroscopy). To validate our methods, perform injection-and-recovery tests using simulated transit photometry over a grid of transit parameters and compare the performance of our proposed T_{14} + importance sampling approach to the performance of the standard $e-\omega-\rho$ modeling basis. We find that the two methods yield equivalent posterior inferences on b , e , and ω , with significant improvements to speed and efficiency when using our new approach. Another major advantage of our proposed technique is that it is “future-proof” in that it allows us to update estimates of e and ω as stellar characterization is inevitably updated in the future (e.g., from new Gaia data releases) without requiring a computationally expensive rerun of the transit fits. In comparison, the usual seven-parameter $e-\omega-\rho$ basis “bakes in” a particular value of ρ_* at the time of transit modeling.

We lay out our methodology for light-curve synthesis and transit injection and recovery in Section 2. We then highlight the procedural differences between the $e-\omega-\rho$ method (Section 3) and our T_{14} method (Section 4). In Section 5, we analyze the results of our injection-and-recovery tests and

compare the performances of the two parameterizations. We provide a summary of our conclusions in Section 6.

2. Synthetic Light-curve Construction

Our objective is to compare the performance of the physical $e-\omega-\rho$ parameter basis to the simpler T_{14} basis. We aim to demonstrate whether or not these methods return equivalent and accurate posterior results and determine their relative efficiencies. To achieve these objectives, we perform a suite of injection-and-recovery tests over a grid of parameters that spans a wide range of values of eccentricity e , argument of periastron ω , inclination (parameterized as impact parameter b), and signal-to-noise ratio (see Figure 1). Injection and recovery is a standard tool used to evaluate transit signal detection methods (see, e.g., Christiansen et al. 2015), but it has not been applied to transit model validation on nearly the same scale. Here, we construct a set of synthetic light curves; then we proceed to use two distinct transit modeling methods to recover the injected transit properties and compare the relative model performances.

For all injection–recovery tests in this work, we inject the transit signal of a sub-Neptune-size planet orbiting a Sun-like star with an orbital period close to the average among Kepler planets. We synthesize 10 transits per light curve with a photometric zero-point flux of $\mu_{\text{flux}} = 0$ and a fixed photometric noise σ_{flux} , consistent with raw photometry that has been accurately pre-whitened. We calculate the duration of each injected transit signal T_{14} according to the following equation from Winn (2010):

$$T_{14} = \frac{P}{\pi} \sin^{-1} \left(\sqrt{\frac{(1+r)^2 - b^2}{\left(\frac{GP^2\rho_*}{3\pi}\right)^{2/3} - b^2}} \right) \frac{\sqrt{1-e^2}}{1+e\sin\omega}. \quad (1)$$

We construct our synthetic light curves at three different S/N levels: S/N $\sim [20, 40, 80]$. We show example light curves for each S/N level in Figure 1. At an S/N of 20, the injected signal has a slightly lower significance compared to the median Kepler planet signal. At the higher-S/N levels of 40 and 80, we seek to identify any differences that emerge between our two models as the transit ingress and egress become more distinct from the photometric noise, making b measurements more precise. From the selected S/N and other injected light-curve properties, we generate Gaussian white noise per light curve centered on σ_{flux} , which we calculate according to:

$$\sigma_{\text{flux}} = \sqrt{\frac{T_{14,\text{true}} N_{\text{transits}}}{t_{\text{exp}}} \frac{r_{\text{true}}^2}{\text{SNR}}}, \quad (2)$$

where N_{transits} is the number of injected transits and t_{exp} is the simulated exposure time of our synthetic light curve. The random seed used to generate the synthetic white noise is unique to each injection–recovery test.

We also assign a unique set of transit parameter values $\{b, e, \omega\}$ for each injection–recovery test, where each of these inputs is drawn from a grid of discrete parameter values (see Figure 1). We specifically choose a parameter grid that emphasizes the region of the parameter space where the $e-\omega-b$ degeneracy is the strongest (see, e.g., Van Eylen & Albrecht 2015) as this is where the two parameterizations are more likely to yield differing results. As a result, our injected planet signals do not exactly mirror the distribution of Kepler

Example: $e = 0.2, b = 0.7$

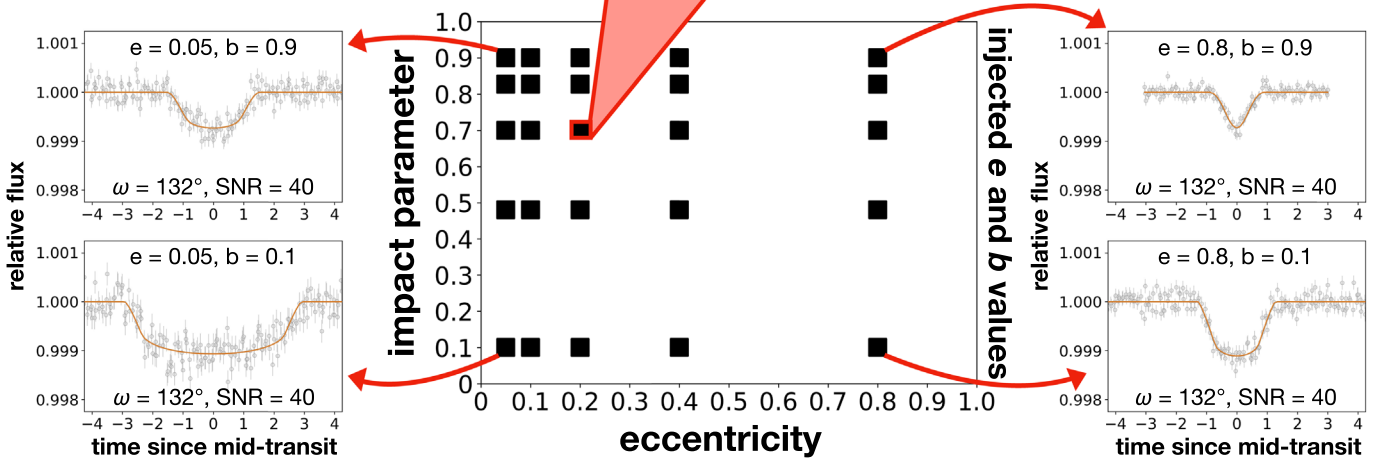
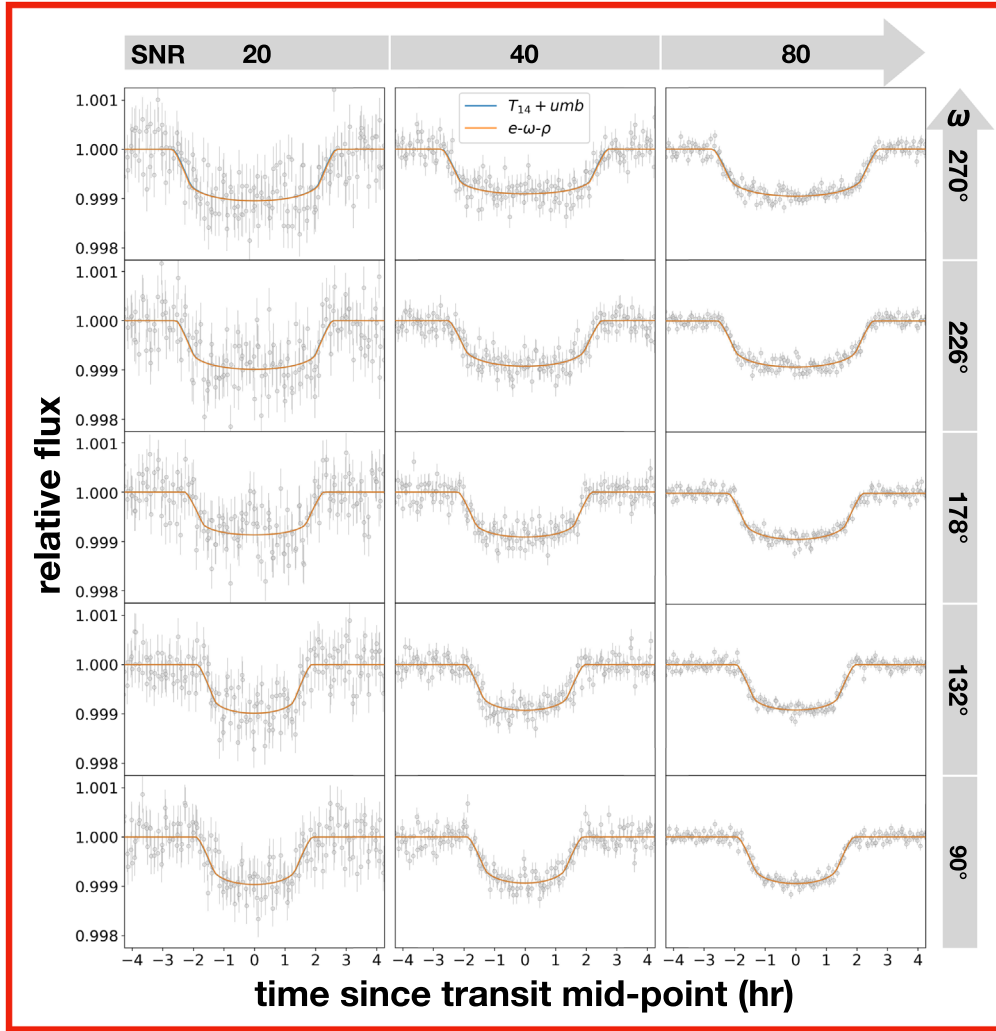


Figure 1. Diagram showing (bottom middle) our grid of injected e and b values, along with (top) a gallery of phase-folded light curves for all combinations of S/N and injected ω values (at $e = 0.2$ and $b = 0.7$, as an example). The four panels to the left and right of the bottom grid show demonstrative examples of phase-folded light curves at the different extremes of our injected parameter grid (e.g., $b = 0.1$ or 0.9 and $e = 0.05$ or 0.8), all shown with $\omega = 132^\circ$ and S/N = 40. Each light curve is shown with the median final transit fits from both the $e-\omega-\rho$ (orange) and $T_{14} + umb$ (blue) modeling methods, which overlap almost entirely.

planets, but they do include a broad range of realistic planet characteristics.

As the transit shape is more sensitive to small changes in b at high values, we select injected values of b with tighter spacing toward higher values, spanning the nongrazing parameter

space. We construct an array of b values that are evenly spaced on a reversed log scale: $b \sim [0.1, 0.48, 0.7, 0.83, 0.9]$. We also prefer to use e values that span the range of eccentricities with tighter spacing toward low-to-moderate values, as these are more common. We select an array of possible e values which

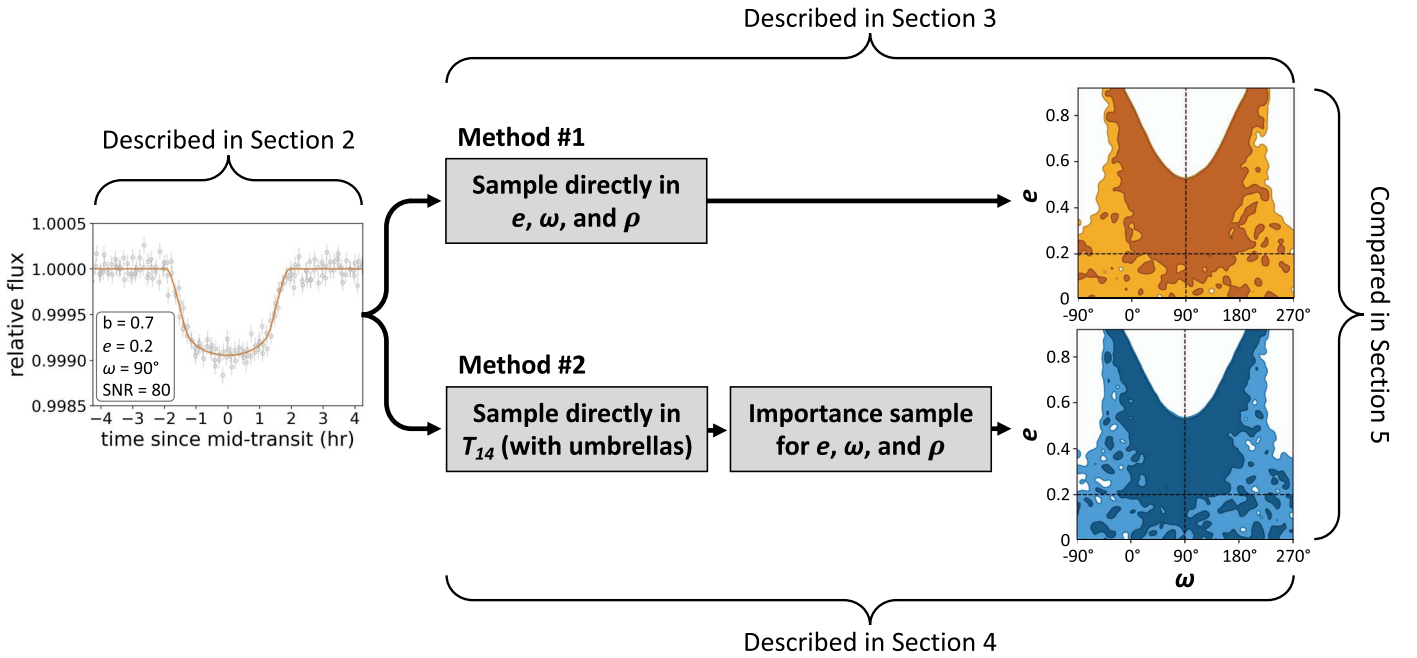


Figure 2. Diagram demonstrating an overview of our modeling procedure, from an input synthetic light curve to output e and ω constraints via both the e - ω - ρ (orange) and T_{14} + umb (blue) modeling methods.

are evenly spaced on a log scale: $e \sim [0.05, 0.1, 0.2, 0.4, 0.8]$. Additionally, the ω values that we draw upon for our grid of injected parameters are intentionally selected to include the inflection points of periastron ($\pi/2$ or 90°) and apastron ($3\pi/2$ or 270°) along with three roughly evenly spaced values between: $\omega \sim [90^\circ, 132^\circ, 178^\circ, 226^\circ, 270^\circ]$.

We construct a set of 375 unique transit light curves from all combinations of $\{b, e, \omega, S/N\}$ using the `batman` transit modeling package (Kreidberg 2015). We synthesize these injected light-curve models with an oversampling rate of 11 and $t_{\text{exp}} = 30$ minutes, similar to real Kepler photometry. These light curves serve as inputs to the two modeling methods that we are comparing, described below, in order to demonstrate similarities and differences in model performance across a range of potential transit signals (see Figure 2 for an overview).

3. Method #1: Direct sampling in e - ω - ρ

We first model our synthetic transit light curves using the e - ω - ρ model, which serves as our baseline model and standard reference when evaluating the performance of our proposed T_{14} + umb model. This physically motivated transit model is parameterized by $\{P, t_0, r, b, \rho_*, e, \omega\}$, along with quadratic limb-darkening parameters $\{u_1, u_2\}$. As we simulate light curves with white noise, we fix μ_{flux} and σ_{flux} which would otherwise be directly sampled parameters when modeling real transit photometry.

We construct the e - ω - ρ model using uninformative priors that are of standard use in transit fitting literature or drawn directly from G22, summarized in Table 1. We apply a normal prior on ρ_* which assumes that the stellar density is known with 10% uncertainty through independent measurements. To mitigate boundary issues that can occur when sampling e and ω directly, we use a common redefinition of these parameters $\{\sqrt{e} \sin \omega, \sqrt{e} \cos \omega\}$ (see, e.g., Eastman et al. 2013), with implicit uniform priors on both e and ω . These priors do not

Table 1
Transit Model Parameters and Priors

Parameter	Input Value(s)	Prior
P (d)	26.1	fixed
t_0 (d)	1.0	$t_0 \sim N(1.0, 0.1)$
r	0.03	$\log r \sim U(-9, 0)$
b	[0.1, 0.48, 0.7, 0.83, 0.9]	$b \sim U(0, 1 + r)$
u_1, u_2	{0.4, 0.25}	fixed
μ_{flux}	0	fixed
σ_{flux}	derived	fixed per light curve
T_{14} (d)	derived	$\log T_{14} \sim U(-9, 0)$
e	[0.05, 0.1, 0.2, 0.4, 0.8]	$e \sim U(0, 0.92)$
ω ($^\circ$)	[90, 132, 178, 226, 270]	$\omega \sim U(-90, 270)$
ρ_* (g/cm^3)	1.41 (e.g., ρ_\odot)	$\rho_* \sim N(1.41, 0.141)$

All parameters used in the models discussed throughout this analysis, along with their units, input values, and associated priors (if applicable). Priors include normal (N) and uniform (U) distributions. b , e , and ω each have five input value options that form a grid of possible injected transit signal properties. We note that the priors on e and ω can also be represented via the transform $\{e, \omega\} \rightarrow \{\sqrt{e} \sin \omega, \sqrt{e} \cos \omega\} \sim \text{Disk}(\sqrt{0.92})$.

account for transit probability or other astrophysically motivated considerations (see Barnes 2007).

We implement this model using `exoplanet` (Foreman-Mackey et al. 2021), with sampling performed by the NUTS algorithm via `PyMC3` (Salvatier et al. 2016). We use 3000 tuning steps with an additional 4000 sampler draws to ensure that the sampler converges with an effective sample size $N_{\text{eff}} \approx 10^3$. We also set a high target acceptance fraction of 0.99 to encourage the sampler to adequately explore complex topologies in the posterior parameter space, such as the $b-r$ and $e-\omega$ degeneracies. We follow the standard practice of oversampling the light-curve model in order to mitigate binning artifacts (see, e.g., Kipping 2010), using an oversampling factor of 11. We fit our transit models via two sampler chains across two CPU cores per injection-recovery test.

From initial experimentation, we found that sampler limitations exist, which restrict the valid parameter space of eccentricity modeling when applying the e - ω - ρ parameterization via NUTS sampling with `exoplanet`. When sampling $e \gtrsim 0.92$, this implementation of the e - ω - ρ model can have convergence issues due to the high curvature of the posterior parameter space being traversed. This also roughly corresponds with the upper eccentricity limit where we expect transit duration approximations to begin breaking down (see, e.g., Kipping 2014). Given that only 5 known planets have $e > 0.9$ and only one of these was discovered via transit modeling, we choose to restrict our eccentricity sampling to $e < 0.92$ for all modeling approaches considered in this work. By doing so, we avoid conflating our primary interest—differences in modeling methods—with rare edge cases that are beyond the scope of this work.

4. Method #2: Direct Sampling in T_{14} , then Importance Sampling in e - ω - ρ

Our alternative transit modeling approach, the $T_{14} + \text{umb}$ model, has a parameter basis that includes the observable transit duration T_{14} as an explicit parameter. This parameterization avoids explicitly sampling the complex degeneracies introduced by e and ω , allowing us to instead measure these parameters post-hoc via importance sampling (see 4.2). We couple this duration-based parameterization with umbrella sampling (see Gilbert 2022) to ensure that our model accurately samples the complicated topology of the high- b “grazing” parameter space. Based on the arguments made in both G22 and Gilbert 2022, we expect that our $T_{14} + \text{umb}$ approach should achieve results that are consistent with those from the e - ω - ρ model with a potential boost in efficiency.

4.1. Transit Fitting

Similar to our implementation of the baseline e - ω - ρ model, we also construct our $T_{14} + \text{umb}$ model via `exoplanet` with NUTS sampling and use it to model our synthetic transit signals. This parameterization is motivated by observable transit properties and characterized by the basis $\{P, t_0, r, b, T_{14}\}$. Like the e - ω - ρ model, the $T_{14} + \text{umb}$ model also includes quadratic limb-darkening parameters $\{u_1, u_2\}$ as well as fixed values of μ_{flux} and σ_{flux} . The priors used here are identical to those used in our e - ω - ρ model, summarized in Table 1. Neither e nor ω is explicitly constrained during the sampling process here, and their values are instead estimated from post-model importance sampling. This parameterization is thus agnostic to orbital eccentricity, except for the implicit assumption of a symmetric transit. This is a reasonable approximation as the acceleration of an eccentric planet during its transit is unlikely to introduce detectable asymmetry given modern photometry (Barnes 2007).

To improve both the sampling convergence and the exploration of complex posterior topologies, we follow Gilbert (2022) to implement umbrella sampling. We separate our NUTS sampler into three windows (i.e., “umbrellas”) defined within the joint $\{r, b\}$ parameter space, which allows us to sample the full posterior parameter space in smaller pieces that are easier to explore. The resulting posteriors can later be stitched together by applying the appropriate umbrella weights. The three umbrella windows that we use correspond to nongrazing and grazing orbits separated by a region that we

refer to as the transition umbrella, which partially overlaps with the other two (see Gilbert 2022 for full description). In our implementation, we apply the three umbrella models in series but emphasize that this task can easily be parallelized to reduce the apparent wall-clock runtime. In the Appendix, we also discuss a potential alternative to umbrella sampling, known as dynamic nested sampling (see, e.g., Skilling 2004; Skilling 2006), which achieves roughly comparable results.

4.2. Importance Sampling

To recover $\{e, \omega\}$ samples from the $T_{14} + \text{umb}$ modeling approach, we apply post-hoc importance sampling to the combined umbrella model posterior distributions. Importance sampling (see, e.g., Oh & Berger 1993; Gilks et al. 1995; Madras & Piccioni 1999) allows one to measure the properties of a given parameter’s probability distribution based on samples generated from a different (typically easier to sample) parameter’s distribution. This method was first incorporated into exoplanet characterization models by Ford 2005 and Ford 2006, used in combination with Markov Chain Monte Carlo (MCMC) sampling to improve radial velocity model efficiency. Such methods can be useful to correct for observational biases post-hoc or derive the distributions of more complicated distributions outside of the MCMC sampling routine. Importance sampling is closely related to umbrella sampling, and the former can be thought of as a single-window special case of the latter. In our implementation, importance sampling only marginally increase the total runtime of the $T_{14} + \text{umb}$ approach by a few seconds.

We first compute the relative weights of the three umbrella models following Gilbert 2022 and combine our posterior chains into a single set of weighted posterior distributions. As the umbrella weights effectively reduce the total number of samples, we upsample the merged posterior distributions via random resampling to generate a total of 10^5 samples per parameter for convenience. We then perform importance sampling to weigh how well the measured values of $\{P, r, b, T_{14}\}$ at each sampler step can be described by an independently measured density of the host star. We will refer to this independent stellar density as $\rho_{*,\text{true}}$, with some uncertainty $\sigma_{\rho_{*,\text{true}}}$. To determine the appropriate importance weights, we first calculate the sampler-derived stellar density, $\rho_{*,\text{samp}}$, at each point in the umbrella-weighted posterior. This calculation directly follows from the transit duration equation described by Winn 2010:

$$\rho_{*,\text{samp}} = \frac{3\pi}{GP^2} \left(\frac{(1+r)^2 - b^2}{\sin^2\left(\frac{T_{14}\pi}{P} \frac{1+e\sin\omega}{\sqrt{1-e^2}}\right)} + b^2 \right)^{3/2}. \quad (3)$$

We note that Equation 3 explicitly includes e and ω , for which we do not yet have any information. We substitute these parameters with random draws of $\{e, \omega\}$ from uniform priors $e \sim U(0, 0.92)$ and $\omega \sim U(-\frac{\pi}{2}, \frac{3\pi}{2})$ —recall that the upper limit $e = 0.92$ was chosen to circumvent sampling issues at high e in the e - ω - ρ basis. By deriving $\rho_{*,\text{samp}}$ from measured values of $\{P, r, b, T_{14}\}$ and random uniform values of $\{e, \omega\}$, we ensure that $\rho_{*,\text{samp}}$ reflects a true stellar density as opposed to the pseudo-stellar density parameterization which assumes $e = 0$ and was deemed unreliable by G22.

We compare the samples of $\rho_{*,\text{samp}}$ against the independently measured $\rho_{*,\text{true}}$ by computing the log-likelihood of each i^{th} sample,

$$\log \mathcal{L}_i = -\frac{1}{2} \left(\frac{\rho_{*,\text{samp},i} - \rho_{*,\text{true}}}{\sigma_{\rho_{*,\text{true}}}} \right)^2, \quad (4)$$

assuming a Gaussian likelihood function. We then weight each sample from our umbrella-weighted posterior distributions by

$$w_i = \frac{\mathcal{L}_i}{\sum_i \mathcal{L}_i} \quad (5)$$

to produce the final, importance-weighted posterior distributions for each parameter. We apply these same weights to the random uniform $\{e, \omega\}$ samples to derive the final posterior distributions of these two parameters. All analysis in this work regarding the $T_{14} + \text{umb}$ model is based on these posterior distributions that have been umbrella-weighted, up-sampled, and importance-weighted. The final posterior distribution of e that we measure using our $T_{14} + \text{umb}$ modeling approach can thus be directly compared to the e posterior from the $e-\omega-\rho$ model.

We therefore can use the T_{14} basis $\{P, t_0, b, r, T_{14}\}$ along with an independently constrained ρ_{true} to derive posterior distributions for all parameters represented by the $e-\omega-\rho$ basis $\{P, t_0, b, r, e, \omega, \rho_*\}$. With the T_{14} basis, we have the advantage of avoiding introducing significant stellar constraints (i.e., ρ_*) until after the transit has already been fully modeled. Thus, our $T_{14} + \text{umb}$ model only needs to be run once while the $e-\omega-\rho$ model would have to be rerun for each updated measurement of stellar density. The post-hoc importance sampling step can easily be rerun for an updated $\rho_{*,\text{true}}$ value (or different priors on e or ω) within only a few seconds, making our $T_{14} + \text{umb}$ modeling approach essentially future-proof. In the era of Gaia and high-precision stellar characterization, such future proofing will become increasingly valuable.

5. Results

5.1. Both Methods Return Equivalent Eccentricity Constraints

We fit 375 injected transit signals from our grid of injection–recovery tests using both the $e-\omega-\rho$ baseline model and our $T_{14} + \text{umb}$ modeling approach. We measure all transit parameters using both modeling approaches, including e and ω . The posterior distributions of e , ω , and b serve as our primary points of comparison between the baseline model and our alternative modeling approach. Here, we specifically focus our analysis on e , as b (and its relationship with r) was already covered in G22 and ω is often a nuisance parameter in photometric modeling. We use posterior comparisons of ω and b for secondary analysis when necessary.

We perform a quantile–quantile comparison of the posterior values e_k at the $k = 15^{\text{th}}$, 50^{th} , and 85^{th} percentiles of the $e_{\omega\rho}$ and $e_{T_{14}+\text{umb}}$ eccentricity distributions. In Figure 3, we present a comparison of e_k from both modeling methods at each of the key percentiles for all injection–recovery tests. We see that all tests at each percentile are close to the one-to-one line (black), demonstrating that the two modeling methods produce nearly equivalent posterior results for e .

We compute the difference Δe_k (e.g., $\Delta e_{50} = e_{50,e\omega\rho} - e_{50,\text{umb}}$) and use this as a measure of similarity between the two model results. To estimate the significance of Δe_k for each posterior

comparison, we assume a standard eccentricity uncertainty of $\sigma_e = 0.05$, informed by the typical uncertainty on e measured among all known planets ($\sigma_{\text{median}}(e) \approx 0.05$; NASA Exoplanet Science Institute 2020²). For injection–recovery tests where $|\Delta e_k| \lesssim 0.05$ at the 15th, 50th, and 85th percentiles of eccentricity, we assert that the $e-\omega-\rho$ and $T_{14} + \text{umb}$ methods produce equivalent results. Among multiple iterations of our suite of injection–recovery tests, we did not identify any tests which consistently produced posterior measurements for e that differed by $|\Delta e_k| \lesssim 0.05$ (see Figure 3). This suggests that our approach is an excellent alternative to the $e-\omega-\rho$ method, as the two methods should converge on identical results (as opposed to $\sim 68\%$ identical).

We also consider how Δe_k differs as a function of both the light-curve S/N and the injected transit duration T_{14} . Specifically, we consider the ratio between T_{14} and the expected duration of the same planet on a circular, centrally transiting orbit (the reference duration, $T_{14,\text{ref}}$): $T_{14}/T_{14,\text{ref}}$. This duration ratio is a more concise metric to interpret the effects of e , ω , and b on the duration of a transit. While we observe no trend in Δe_k with respect to S/N, we do note a marginal trend in Δe_k as a function of $T_{14}/T_{14,\text{ref}}$ across our sample. We find that the $T_{14} + \text{umb}$ model estimates slightly higher e values than the $e-\omega-\rho$ model at short transit durations and vice-versa at long transit durations, but the deviations that contribute to this trend are sub-significant. We ultimately conclude that the two modeling methods produce equivalent eccentricity measurements (within a reasonable uncertainty) for virtually all tenable combinations of $\{e, \omega, b, \text{S/N}\}$.

5.2. Both Methods Return Accurate Results

We have demonstrated that our alternative transit modeling approach produces equivalently accurate results relative to our baseline model, but we have not yet considered if these models yield the correct results (relative to the injected parameters). It is known in the field of exoplanet characterization that photometric eccentricity constraints (and ω constraints) tend to have large uncertainties for individual planets (see, e.g., Van Eylen et al. 2019). Here, we qualitatively assess these uncertainties across our set of injection–recovery tests.

As our sample is not representative of the observed planet population, we describe the observed trends among our e measurements according to different quadrants of $e-b$ parameter space. We split up our tests into four broad scenarios based on their injected transit properties: (1) low e and low b , (2) low e and high b , (3) high e and low b , (4) high e and high b . We show demonstrative examples of these four scenarios in Figure 4 with several ω values, all at S/N = 20. In all four quadrants, the posterior distributions of e and b are broad, non-Gaussian, and display a range of outcomes, but we describe the general trends that we observe below. We also offer some additional discussion regarding how ω can affect these posterior constraints. We limit our discussion to only the posterior distributions of the $T_{14} + \text{umb}$ modeling approach as the two approaches produce nearly equivalent results.

In scenario 1 (low e and low b), transit models accurately measure low values for both e and b with little posterior mass at higher values (Figure 4, top left), regardless of ω . In scenario 2 (low e and high b), models tend to significantly overestimate e but produce more accurate measurements of b (Figure 4,

² NASA Exoplanet Archive data retrieved on 2023 February 23

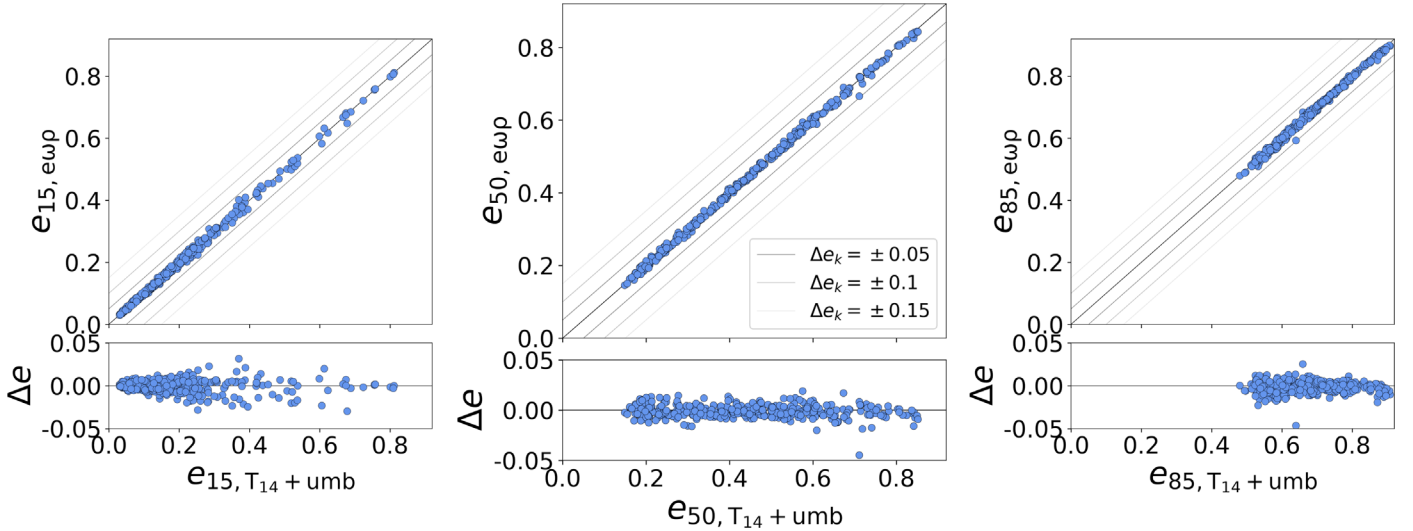


Figure 3. Comparison of e values measured from the $T_{14} + \text{umb}$ and $e-\omega-\rho$ modeling methods at the 15th, 50th, and 85th percentiles of their distributions, along with the residuals Δe_k for each comparison (e.g., $\Delta e_{50} = e_{50,ewp} - e_{50,umb}$). We show $\Delta e_k = \{0.05, 0.1, 0.15\}$ in gray, as well as the ideal 1-to-1 line shown in black. These comparisons generally lie close to the 1-to-1 line, implying that the results of the two models are approximately equivalent. We see no trends in the residuals of these comparisons.

bottom left), regardless of ω . The opposite is true in scenario 3 (high e and low b), where b tends to be overestimated while e is measured more accurately (Figure 4, top right), except near apastron where both are measured fairly accurately. In scenario 4 (high e and high b), transit models tend to accurately measure high values for both parameters with little posterior mass at lower values (Figure 4, bottom right), except near apastron where neither is measured well. We avoid providing a quantitative description of these observed trends because the non-Gaussian posterior distributions are not well-represented by simple summary statistics.

When e is high (e.g., scenarios 3 and 4), the value of ω_{true} can significantly impact the posterior constraints on e and b due to the degenerate influence that these parameters can have on the observed transit duration, particularly near apastron. On the other hand, we do not observe any noteworthy trends in model accuracy as a function of S/N. For a typical Kepler planet, which has low e , nongrazing b , and ω closer to periastron, we would generally expect to measure e and b posterior distributions that are somewhat consistent with the true underlying orbital geometry of the planet based on the trends that we observe in Figure 4. In Appendix B, we briefly explore whether using a different sampler (i.e., dynamic nested sampling via *dynesty*; Speagle 2020) might yield even more accurate posterior constraints, but our findings there are inconclusive.

5.3. Our $T_{14} + \text{umb}$ Method is More Efficient than the $e-\omega-\rho$ Method

We have shown that the $T_{14} + \text{umb}$ basis can be used as an alternative to the $e-\omega-\rho$ basis, achieving equivalent results while also reducing the number of parameters by two. This parameter reduction should increase the efficiency of the $T_{14} + \text{umb}$ model, but this approach also requires three separate sampling runs—one for each of the three umbrellas. To evaluate the overall model efficiencies, we compared the number of effective samples per second (η) achieved by each method for all injection–recovery tests.

For the $e-\omega-\rho$ method, we measure the number of effective samples from the r posterior distribution for each test using Geyer’s initial monotone sequence criterion via *arviz* (Geyer 1992; Gelman et al. 2013; Kumar et al. 2019). We select r because it is a common output between our models and is less affected by complicated parameter degeneracies. We then divide N_{eff} by the total runtime for this model to achieve the $e-\omega-\rho$ sampling efficiency, $\eta_{e\omega\rho}$. For the $T_{14} + \text{umb}$ method, we average N_{eff} of the r posteriors from each umbrella model, weighted by their respective umbrella weights. We divide this weighted average by the sum of the runtimes for the three umbrella models (e.g., the CPU runtime) to achieve the overall $T_{14} + \text{umb}$ sampling efficiency, $\eta_{T_{14}+\text{umb}}$.

We calculate the ratio of these two efficiencies for all injection–recovery tests and find that $\eta_{T_{14}+\text{umb}}/\eta_{e\omega\rho} > 1$ for $\sim 73\%$ of tests, suggesting that the $T_{14} + \text{umb}$ approach is generally more efficient across our set of injected planet parameters. The median value of $\eta_{T_{14}+\text{umb}}/\eta_{e\omega\rho}$ across our sample is 2.0, implying that the $T_{14} + \text{umb}$ approach is typically 2 \times more efficient than the $e-\omega-\rho$ method, although the range of this efficiency ratio is broad. When we consider $\eta_{T_{14}+\text{umb}}/\eta_{e\omega\rho}$ as a function of S/N, however, we measure a median efficiency increase of $5.7\times$ at S/N = 80, $1.2\times$ at S/N = 40, and $1.1\times$ at S/N = 20 (see Figure 5). We also find that the $T_{14} + \text{umb}$ method is only more efficient than the $e-\omega-\rho$ method in $\sim 52\%$ of low-S/N tests. These findings suggest that the $T_{14} + \text{umb}$ method tends to be less efficient when the transit signal is weaker.

From Figure 5, we also see that the efficiency ratio changes with respect to the duration ratio $T_{14}/T_{14,\text{ref}}$. For tests with S/N = 20, the median efficiency ratio $\eta_{T_{14}+\text{umb}}/\eta_{e\omega\rho}$ decreases significantly as the duration ratio increases, dropping from $2.1\times$ at $T_{14}/T_{14,\text{ref}} \leq 0.8$ to $0.6\times$ at $T_{14}/T_{14,\text{ref}} > 0.8$. This trend is likely due to differences in how the two methods explore the high- b grazing regime. As the duration ratio approaches unity or higher, high b values are significantly less likely, but the $T_{14} + \text{umb}$ approach continues to carefully explore the high- b regime via three umbrella models even when it is not necessary. On the other hand, injection–recovery tests with

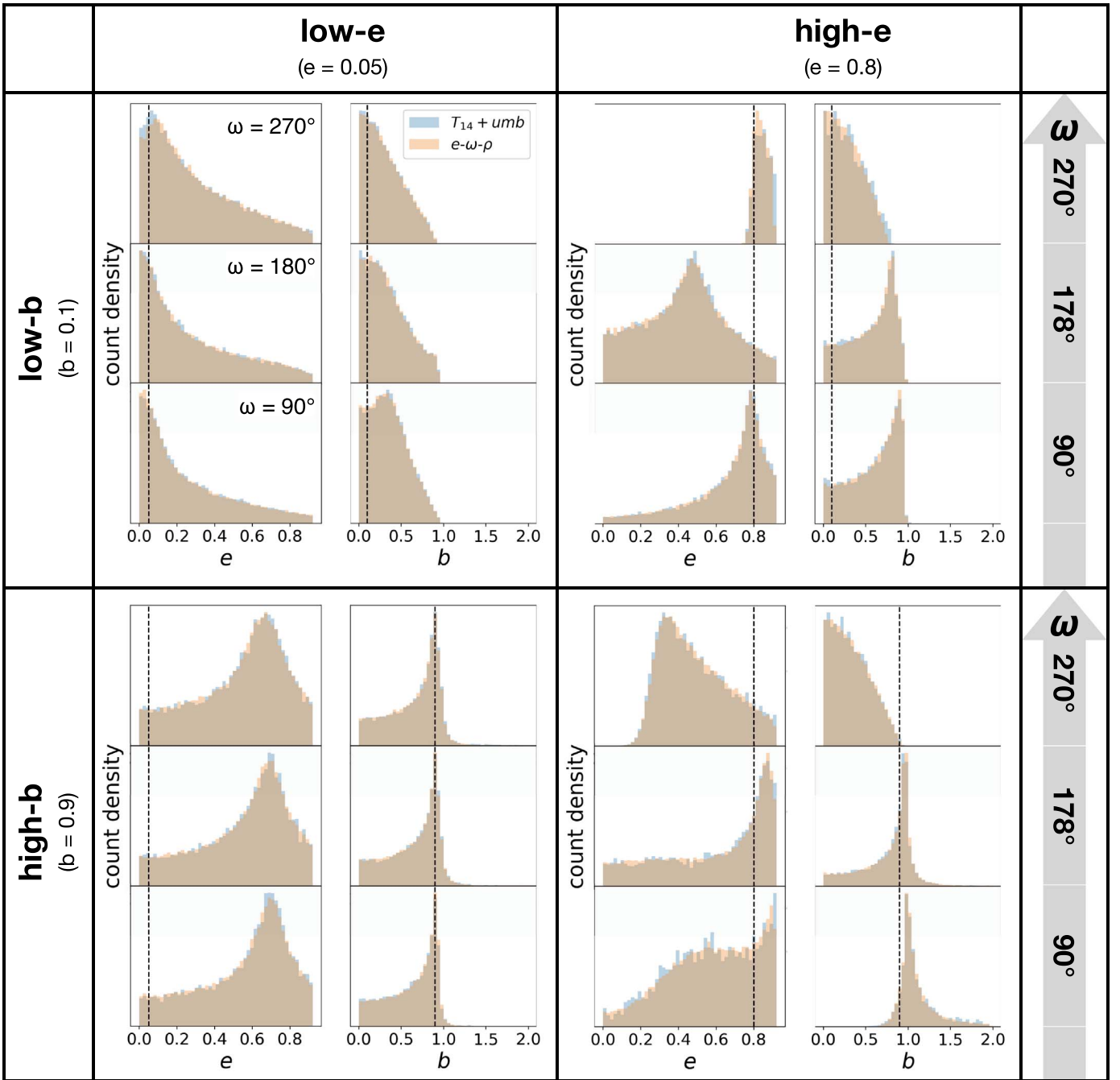


Figure 4. Qualitative diagram showing the relative accuracy of measuring e and b from transit photometry in four distinct quadrants of the e – b parameter space, at three different ω values. The four scenarios shown are (top left) low e and low b , (bottom left) low e and high b , (top right) high e and low b , and (bottom right) high e and high b . Across all areas of the e – b parameter space, the $T_{14} + \text{umb}$ (blue) and e – ω – ρ (orange) modeling methods perform equivalently.

higher b values (and generally shorter transit durations) are more efficiently sampled by the $T_{14} + \text{umb}$ approach. This behavior is consistent with what we would expect, given that umbrella sampling is specifically intended to ensure accurate measurements of the high- b parameter space.

Our set of injected transit properties, however, is not completely representative of observed planet demographics. To make a more representative comparison, we estimate the efficiency ratio for a typical Kepler planet based on both S/N and duration ratio $T_{14}/T_{14,\text{ref}}$. We use the latter metric because it reflects the combined effects of e , b , and ω in a single variable. For a typical confirmed Kepler planet with S/N

≈ 20 – 40 and $T_{14}/T_{14,\text{ref}} \approx 0.6$ – 1.1 , we estimate an efficiency ratio of $\sim 0.9\times$. Based on these findings, we assert that the two methods generally have similar sampling efficiencies for real planetary transit signals, with the $T_{14} + \text{umb}$ approach excelling for signals with higher S/N or lower duration ratio.

The efficiency increase from the $T_{14} + \text{umb}$ approach is more significant when we consider wall-clock time rather than CPU time. As the three umbrella models can be run in parallel, we can reduce the apparent runtime of the $T_{14} + \text{umb}$ approach by up to a factor of a few. In this parallelized case, the apparent sampling efficiency of the $T_{14} + \text{umb}$ method is $\sim 1.2\times$ faster than the e – ω – ρ method for a typical Kepler planet. As another

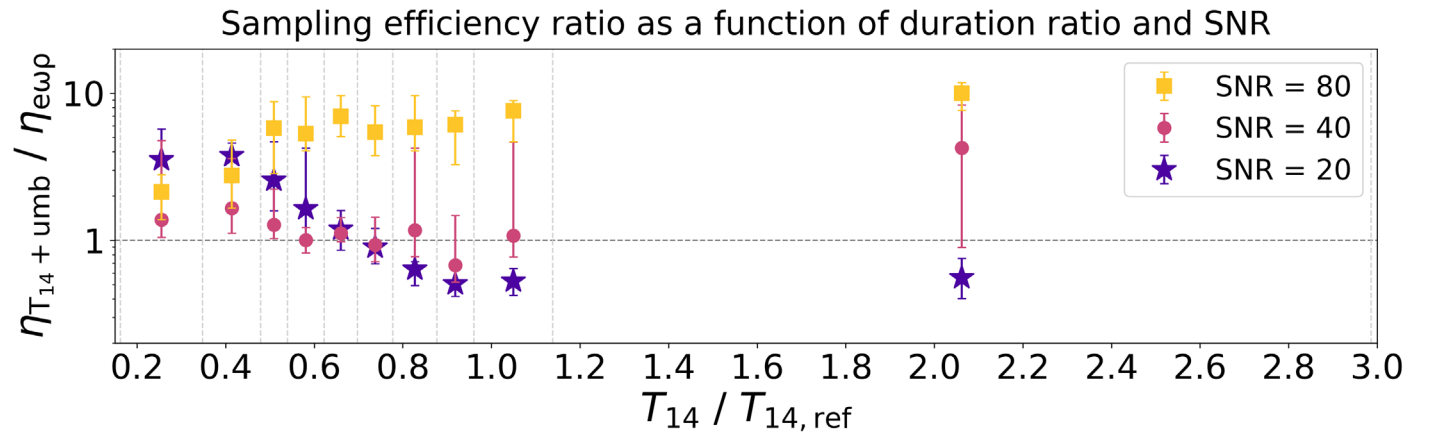


Figure 5. Ratio of sampling efficiencies $\eta_{T_{14} + \text{umb}} / \eta_{e-\omega-\rho}$ as a function of the duration ratio $T_{14} / T_{14, \text{ref}}$ and S/N. We bin the data across every 10th percentile of the duration ratio distribution, showing a single point per bin per S/N (bins are separated by vertical gray lines). Each point shows the 15th, 50th, and 85th percentiles of a given bin. The increased efficiency of the $T_{14} + \text{umb}$ method relative to the $e-\omega-\rho$ method depends on the S/N of the modeled light curve. At higher S/N the $T_{14} + \text{umb}$ method is significantly more efficient, but at moderate-to-low S/N the two methods have more similar efficiencies. At shorter transit durations, the $T_{14} + \text{umb}$ method is always more efficient, but this behavior changes around $T_{14} / T_{14, \text{ref}} \approx 0.8$. The large spread in some uncertainties reflects the heterogeneity of our injected light-curve parameters.

added benefit, the posteriors of the $T_{14} + \text{umb}$ approach can be importance sampled for updated values of ρ_* (as they become available) without re-running the NUTS sampling process (see Section 4.2), which is a major advantage in the long-term efficiency of the $T_{14} + \text{umb}$ parameterization.

6. Conclusions

In this work, we presented an updated photoeccentric transit modeling method using a duration-based parameterization $\{P, t_0, r, b, T_{14}\}$ (with umbrella sampling) and post-hoc importance sampling which efficiently achieves accurate constraints on e , ω , and b . Through a suite of synthetic injection-and-recovery tests, we demonstrated that our approach produces equivalent eccentricity constraints relative to the more common eccentricity-explicit transit model parameterization $\{P, t_0, r, b, e, \omega, \rho\}$. We find that our modeling method generally has a higher sampling efficiency than the $e-\omega-\rho$ method when the true e or b value is high or a similar efficiency otherwise. Our approach can also be parallelized to increase its relative sampling efficiency several-fold more.

A key advantage of our modeling method is that post-hoc importance sampling allows us to successfully derive accurate e and ω posterior distributions (relative to the $e-\omega-\rho$ method) without including e , ω , or ρ as explicit model parameters. Our importance sampling routine is fast and flexible enough to easily incorporate an updated prior on e and/or ω , which is critical for hierarchical modeling approaches at the population level. Our method also allows us to update parameter posterior distributions according to updated values of ρ_* (e.g., from new Gaia data releases) without any loss of generality. In the modern era of high-precision stellar characterization, this sort of “future proofing” will be invaluable as the number of transit candidates around well-characterized stars continues to grow.

Acknowledgments

We are grateful to Dan Foreman-Mackey for helpful conversations about this work. This study made use of computational resources provided by the University of California, Los Angeles and the California Planet Search.

G.J.G., M.G.M., and E.A.P. acknowledge support from NASA Astrophysics Data Analysis Program (ADAP) grant (80NSSC20K0457). E.A.P. acknowledges support from the Alfred P. Sloan Foundation. M.G.M acknowledges support from the UCLA Cota-Robles Graduate Fellowship.

Facility: Kepler

Software: `astropy` (Collaboration et al. 2018), `exoplanet` (Foreman-Mackey et al. 2021), `numpy` (Harris et al. 2020), `PyMC` (Salvatier et al. 2016), `scipy` (Virtanen et al. 2020), `batman` (Kreidberg 2015), `arviz` (Kumar et al. 2019), `dynesty` (Speagle 2020)

Appendix A Sampling Methods

Modeling transit photometry requires efficient exploration of the joint posterior parameter space for some number of transit parameters. A higher number of parameters typically increases the complexity of the posterior space and decreases modeling efficiency. Various tools have been developed for sampling from these complicated posteriors, which we employ and compare throughout this work.

In this section, we briefly review several sampling techniques. This review is not intended to be exhaustive but rather serves as a jumping-off point for readers who may be unfamiliar with one or more methods explored in this work.

A.1. Importance Sampling

Importance sampling (see, e.g., Oh & Berger 1993; Gilks et al. 1995; Madras & Piccioni 1999) allows one to measure the properties of given parameter’s probability distribution based on samples generated from a different (typically easier to sample) parameter’s distribution. This method was first incorporated into exoplanet characterization models by Ford (2005) and Ford (2006), used in combination with MCMC sampling to improve radial velocity model efficiency. Such methods can be useful to correct for observational biases post-hoc or derive the distributions of more complicated distributions outside of the MCMC sampling routine. Importance sampling is closely related to umbrella sampling (see

Section A.2), and the former can be thought of as a special case of the latter.

A.2. Umbrella Sampling

A critical challenge for any sampling problem is knowing when (and if) the posterior space has been fully explored. Even the most sophisticated sampling algorithms may fail to find isolated modes or explore the long tails of distributions. Moreover, convergence tests may offer no hint that portions of the parameter space have been missed. In order to ensure proper sampling, one may adopt umbrella sampling (Torrie & Valleau 1977; Kästner 2011), which manually forces the sampler to consider all parts of the posterior topology.

The core idea behind umbrella sampling is straightforward: rather than sampling from a pathological posterior using a single chain (or set of live points), we break the problem into smaller more manageable pieces (“windows,” in the standard nomenclature), sample from the subdistributions independently, and then recombine the subsamples into a single joint posterior distribution after the fact. As long as all subdistributions are adequately sampled, umbrella sampling will return results that are at least as good as those obtained through standard methods, and often better. Umbrella sampling does not replace other sampling methods, but rather works in tandem with them as a meta-strategy for guiding the sampling problem. Umbrella sampling was introduced into the astrophysics literature by Matthews et al. (2018) and adapted to the problem of exoplanet transits by Gilbert (2022).

Appendix B

Sampler Comparison: NUTS Versus Nested Sampling

In the previous sections, we demonstrated that the baseline $e-\omega-\rho$ model and our alternative $T_{14} + \text{umb}$ approach yield equivalent results when posterior samples are obtained using MCMC methods. Unfortunately, we also saw that posterior inferences of eccentricity can be significantly overestimated or

underestimated relative to their true values. Here, we explore whether using a different sampling technique—dynamic nested sampling (Skilling 2004; Skilling 2006)—can yield more accurate results and/or serve as a potential alternative to NUTS sampling with umbrella sampling.

We implement the duration-based parameterization using the `dynesty` framework for dynamic nested sampling (Speagle 2020), which does not necessitate the use of umbrella sampling because it already accomplishes the same goal of thoroughly exploring complicated posterior topologies. To model the transit shape and measure the log-likelihood at each sampler step, we use a modified version of `batman` which takes $\{P, t_0, r, b, T_{14}\}$ as explicit transit parameters (in contrast to the default set $\{P, t_0, r, b, e, \omega, \rho_*$). As before, we perform post-hoc importance sampling to obtain $\{e, \omega, \rho_*$ samples. We apply this alternative modeling method, $T_{14} + \text{dyn}$, to all 375 injection–recovery tests in an identical manner as the previous models.

B.1. Posterior Comparison

For each injection–recovery test, we measure the values $e_{k, T_{14} + \text{dyn}}$ from the $T_{14} + \text{dyn}$ eccentricity posterior at the $k = 15\text{th}, 50\text{th}, \text{ and } 85\text{th}$ percentiles of the distribution and compare to the results of the $T_{14} + \text{umb}$ method like in Section 5.1 (Figure 6). We find that the $T_{14} + \text{umb}$ and $T_{14} + \text{dyn}$ methods yield eccentricity results that are broadly in agreement. However, there appears to be more differences between samplers ($T_{14} + \text{umb}$ versus $T_{14} + \text{dyn}$) than between parameterizations ($T_{14} + \text{umb}$ versus $e-\omega-\rho$). The comparison between parameterizations yielded no test results that consistently differed by $|\Delta e_k| \geq 0.05$, but the comparison between samplers yields 42 of such discrepancies. Among these, there are three tests that differ by $|\Delta e_k| \geq 0.15$ and yield entirely different posterior topologies for e .

The discrepant measurements of Δe_k are most common at the $k = 15\text{th}$ percentile, implying that the two sampling methods differ most at sampling the low- e tail of the

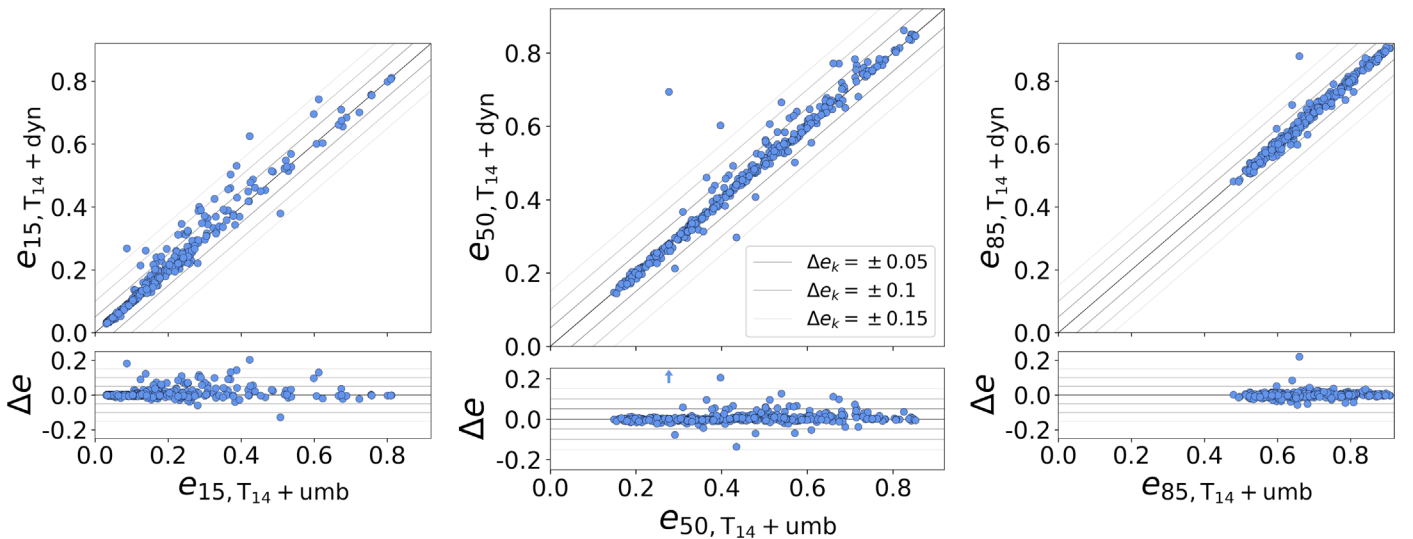


Figure 6. Comparison of e values measured from the $T_{14} + \text{umb}$ and $T_{14} + \text{dyn}$ modeling methods at the 15th, 50th, and 85th percentiles of their distributions, along with the residuals Δe_k for each comparison (e.g., $\Delta e_{50} = e_{50, \text{dyn}} - e_{50, \text{umb}}$). One outlier residual lies beyond the bounds of our residual plots, as indicated by the arrow pointing toward the outlier at $\Delta e_{50} = 0.417$. We show the $\Delta e_k = \{0.05, 0.1, 0.15\}$ in gray, as well as the ideal 1-to-1 line shown in black. These comparisons generally lie close to the 1-to-1 line, implying that the results of the two models are approximately equivalent. However, we do observe 42 tests where the $T_{14} + \text{umb}$ and $T_{14} + \text{dyn}$ model results are discrepant by more than $|\Delta e_k| \gtrsim 0.05$. In these instances, we find that the $T_{14} + \text{dyn}$ model tends to overestimate e relative to the $T_{14} + \text{umb}$ model, as seen in the residuals and discussed in Section B.1.

eccentricity distribution. We observe that the $T_{14} + \text{dyn}$ method produces e posterior distributions with much less posterior weight in the low- e tail as compared to the results of the $T_{14} + \text{umb}$ approach. We also see a similar divergence of the two methods in the upper tail of the b posterior distributions. This is consistent with our additional observation that the majority of the discrepancies occur in tests with shorter duration ratios ($T_{14}/T_{14,\text{ref}} \lesssim 0.5$). Most discrepancies also occur at higher S/N levels, counter to expectations. Together, these criteria for discrepant results only match with $\sim 1\%$ of observed Kepler transit signals, implying that real systems are highly unlikely to fall into this subset.

B.2. Accuracy

We compare the true underlying eccentricity of each injection–recovery test with the measured posterior distribution of e from the $T_{14} + \text{dyn}$ modeling method. Overall, we find that the qualitative trends in e and b measured via the $T_{14} + \text{dyn}$ method are roughly equivalent to those measured from the $T_{14} + \text{umb}$ method (see Section 5.2). We do, however, find a significant difference between the accuracies of the two modeling methods among the three most discrepant injection–recovery tests, where $|\Delta e_{50}| \geq 0.15$. For these discrepant tests, seen as outliers in Figure 6, the $T_{14} + \text{dyn}$ method achieves more accurate posterior constraints on both e and b . This may suggest that differences between samplers can, in some cases, lead to significant differences in the accuracy of modeled parameters. While all three of these tests have $e_{\text{true}} = 0.8$, we unfortunately do not find any discernible rules

by which to distinguish when sampler differences will lead to substantial differences in the accuracy of posterior results.

B.3. Efficiency

We also compare these two modeling approaches according to their sampling efficiencies. We calculate the efficiency $\eta_{T_{14}+\text{dyn}}$ of the $T_{14} + \text{dyn}$ approach for each injection–recovery test, based on the number of effective samples measured via the Kish (1965) approach using `dynesty`. Similar to Section 5.3, we compute the efficiency ratio between the $T_{14} + \text{dyn}$ model and our $T_{14} + \text{umb}$ approach ($\eta_{T_{14}+\text{umb}}/\eta_{T_{14}+\text{dyn}}$) and show these results in Figure 7. The distribution of efficiency ratios among our sample is broad but suggests that the two methods generally have similar sampling efficiencies, with a median efficiency ratio of $\eta_{T_{14}+\text{umb}}/\eta_{T_{14}+\text{dyn}} \approx 1.1$. At lower duration ratios, the $T_{14} + \text{umb}$ approach is $\sim 1.4\times$ more efficient, which is to be expected as this part of the parameter space includes higher b values—the specialty of umbrella sampling as implemented by Gilbert (2022).

For a typical Kepler planet, however, we estimate that the $T_{14} + \text{dyn}$ method is $\sim 1.6\times$ faster than the $T_{14} + \text{umb}$ approach. This observation, along with an occasional improvement in accuracy, leans in favor of dynamic nested sampling compared to NUTS sampling + umbrella sampling for our tests, but there are many other compounding factors that are beyond the scope of our experiment. Overall, both sampling methods offer their own benefits with neither winning out 100% of the time, but it is clear that the duration-based parameterization performs well regardless of the underlying sampling method.

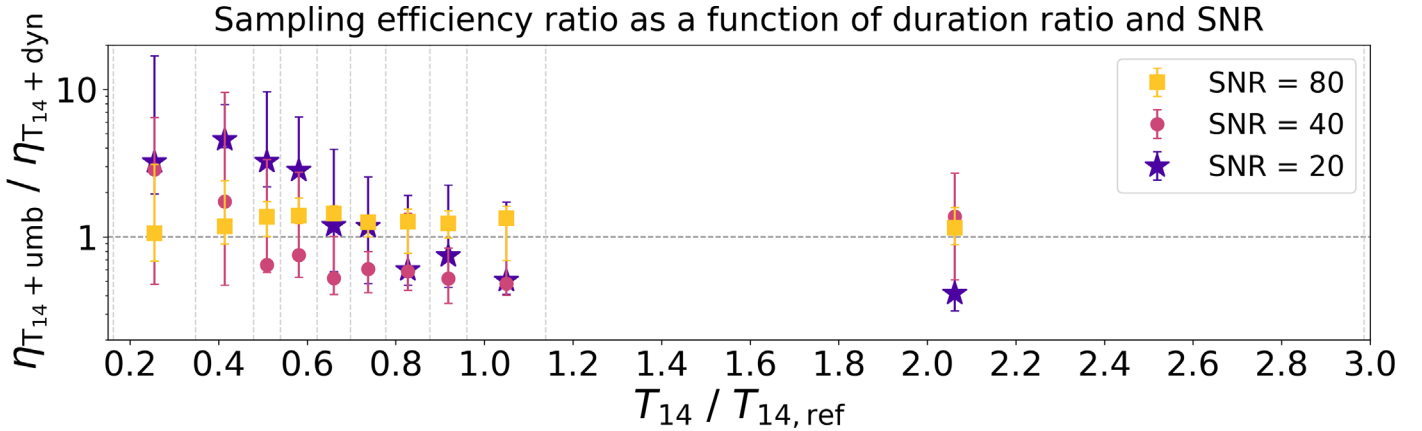


Figure 7. Ratio of sampling efficiencies $\eta_{T_{14}+\text{umb}}/\eta_{T_{14}+\text{dyn}}$ as a function of the duration ratio $T_{14}/T_{14,\text{ref}}$ and S/N. We bin the data across every 10th percentile of the duration ratio distribution, showing a single point per bin per S/N (bins are separated by vertical gray lines). Each point shows the 15th, 50th, and 85th percentiles of a given bin. The efficiency of the $T_{14} + \text{umb}$ method relative to the $T_{14} + \text{dyn}$ method depends partially on the S/N of the modeled light curve. At shorter transit durations, the $T_{14} + \text{umb}$ method is typically more efficient, but the opposite is true at longer transit durations. The large spread in some uncertainties reflects the heterogeneity of our injected light-curve parameters.

ORCID iDs

Mason G. MacDougall  <https://orcid.org/0000-0003-2562-9043>
 Gregory J. Gilbert  <https://orcid.org/0000-0003-0742-1660>
 Erik A. Petigura  <https://orcid.org/0000-0003-0967-2893>

References

- Barnes, J. W. 2007, *PASP*, **119**, 986
 Carter, J. A., Yee, J. C., Eastman, J., Gaudi, B. S., & Winn, J. N. 2008, *ApJ*, **689**, 499
 Christiansen, J. L., Clarke, B. D., Burke, C. J., et al. 2015, *ApJ*, **810**, 95
 Collaboration, Astropy, Price-Whelan, A. M., Sipőcz, B. M., et al. 2018, *AJ*, **156**, 123
 Dawson, R. I., & Johnson, J. A. 2012, *ApJ*, **756**, 122
 Eastman, J., Gaudi, B. S., & Agol, E. 2013, *PASP*, **125**, 83
 Feroz, F., & Hobson, M. P. 2008, *MNRAS*, **384**, 449
 Ford, E. B. 2005, *AJ*, **129**, 1706
 Ford, E. B. 2006, *ApJ*, **642**, 505
 Foreman-Mackey, D., Hogg, D. W., Lang, D., & Goodman, J. 2013, *PASP*, **125**, 306
 Foreman-Mackey, D., Luger, R., Agol, E., et al. 2021, *JOSS*, **6**, 3285
 Gelman, A., Carlin, J., Stern, H., et al. 2013, *Bayesian Data Analysis* (3rd edn.; New York: Chapman and Hall) <https://books.google.com/books?id=ZXL6AQAQBAJ>
 Geyer, C. J. 1992, *StaSc*, **7**, 473
 Gilbert, G. J. 2022, *AJ*, **163**, 111
 Gilbert, G. J., MacDougall, M. G., & Petigura, E. A. 2022, *AJ*, **164**, 92
 Gilks, W., Richardson, S., & Spiegelhalter, D. 1995, *Markov Chain Monte Carlo in Practice* (New York: Chapman and Hall) http://books.google.com/books?id=TRXrMWY_i2IC
 Gaia Collaboration, Brown, A. G. A., & Vallenari, A. 2018, *A&A*, **616**, A1
 Harris, C. R., Millman, K. J., van der Walt, S. J., et al. 2020, *Natur*, **585**, 357
 Kästner, J. 2011, *WIREs Comput. Mol. Sci.*, **1**, 932
 Kipping, D. M. 2010, *MNRAS*, **407**, 301
 Kipping, D. M. 2014, *MNRAS*, **440**, 2164
 Kish, L. 1965, *Am. Polit. Sci. Rev.*, **59**, 1025
 Kreidberg, L. 2015, *PASP*, **127**, 1161
 Kumar, R., Carroll, C., Hartikainen, A., & Martin, O. 2019, *JOSS*, **4**, 1143
 Madras, N., & Piccioni, M. 1999, *Ann. Appl. Probab.*, **9**, 1202
 Matthews, C., Weare, J., Kravtsov, A., & Jennings, E. 2018, *MNRAS*, **480**, 4069
 NASA Exoplanet Science Institute 2020, Planetary Systems Composite Table, IPAC, doi: [10.26133/NEA13](https://doi.org/10.26133/NEA13)
 Oh, M., & Berger, J. 1993, *JASA*, **88**, 450
 Petigura, E. A. 2020, *AJ*, **160**, 89
 Salvatier, J., Wiecki, T. V., & Fonnesbeck, C. 2016, *PeerJ Comput. Sci.*, **2**, e55
 Seager, S., & Mallén-Ornelas, G. 2003, *ApJ*, **585**, 1038
 Skilling, J. 2004, in *AIP Conf. Ser. 735, Bayesian Inference and Maximum Entropy Methods in Science and Engineering: 24th International Workshop on Bayesian Inference and Maximum Entropy Methods in Science and Engineering*, ed. R. Fischer, R. Preuss, & U. V. Toussaint (Melville, NY: AIP), 395
 Skilling, J. 2006, *BayAn*, **1**, 833
 Speagle, J. S. 2020, *MNRAS*, **493**, 3132
 Thompson, S. E., Coughlin, J. L., Hoffman, K., et al. 2018, *ApJS*, **235**, 38
 Torrie, G. M., & Valleau, J. P. 1977, *JCoPh*, **23**, 187
 Van Eylen, V., & Albrecht, S. 2015, *ApJ*, **808**, 126
 Van Eylen, V., Albrecht, S., Huang, X., et al. 2019, *AJ*, **157**, 61
 Virtanen, P., Gommers, R., Oliphant, T. E., et al. 2020, *NatMe*, **17**, 261
 Winn, J. 2010, arXiv:1001.2010